

Ultrafast coherent excitation and probing of molecular vibrations with isotopic substructure

A. Laubereau, G. Wochner, and W. Kaiser

Physik-Department der Technischen Universität München, München, West Germany

(Received 30 December 1975)

Adjacent vibrational modes of different isotope species are coherently excited by an intense ultrashort light pulse. The free decay of the vibrational system is observed by coherent probe scattering of a second delayed interrogating pulse. Coherent superposition of the excited vibrational states gives rise to a beating effect of the collectively vibrating isotope components. The phenomenon is observed for the first time in several tetrahalides on a time scale of several 10^{-12} sec. The experimental information obtained by the probing technique depends on the wave-vector geometry of the material excitation and the interrogating pulse: One individual vibrational component is studied under a selective \vec{k} condition while coherent superposition of the vibrational components is observed for nonselective \vec{k} matching. Our technique provides new information on the vibrational system which is not obtained by other experimental methods.

I. INTRODUCTION

In a series of papers it has been recently demonstrated that molecular vibrations in liquids are effectively excited by ultrashort light pulses.¹⁻⁶ Two aspects of the vibrational excitation were investigated yielding different information on the vibrational dynamics of the system. Observation of the excess population of the upper vibrational state gave for the first time values of the energy relaxation time (population lifetime) in the electronic ground state.¹ From measurements of the coherent vibrational excitation $\langle q \rangle^2$, on the other hand, the vibrational dephasing time τ was directly determined.⁴ For a number of liquids the dephasing time fully accounts for the vibrational linewidth observed in spontaneous Raman spectroscopy.^{7,8} Additional line-broadening mechanisms do not contribute significantly to these vibrational modes.

In this paper more complicated molecular vibrations with considerable overlap between adjacent components will be investigated. Such a situation occurs, for example, for vibrational modes with isotopic components, where the isotope structure often cannot be resolved by spontaneous spectroscopy.⁹ New possibilities of the coherent excitation of inhomogeneously broadened, multiple structured bands will be discussed theoretically and experimentally. It will be shown that a strong phase correlation between adjacent vibrational modes is established by the transient stimulated Raman excitation process. This specific preparation of the molecules gives rise to an interesting beating phenomenon between the individual vibrational modes during the subsequent relaxation. We report on the first experimental observation of such a beating effect between different isotope species of several tetrachlorides.

Experimentally the coherent anti-Stokes Raman scattering of weak probing light pulses¹⁰ was measured. Very important in our investigations is the wave-vector condition (\vec{k} matching) in the stimulated excitation and in the coherent probing process. It will be shown that high selectivity in \vec{k} space can be experimentally achieved by the coherent probing process. As a result, individual isotope species in the sample are readily studied. We have investigated the dephasing time of individual molecular species in isotope mixtures with natural abundances. Experimental data will be presented for vibrational systems where the isotopic line structure cannot be resolved in spontaneous Raman spectroscopy. These results demonstrate the high resolution potential of our picosecond technique which allows us to study the physical event of interest simultaneously in time and \vec{k} space.

II. TRANSIENT STIMULATED RAMAN EXCITATION OF ADJACENT VIBRATIONAL MODES

We have carried out a theoretical investigation of transient stimulated Raman scattering of neighboring vibrational levels. The present discussion extends a previous treatment¹⁰ for a single vibrational transition to the case of several molecular species, e.g., isotope components.

We start with the description of the electromagnetic fields. The propagation of the light pulses through the sample and the interaction with the vibrating molecules is represented by the nonlinear wave equation

$$\Delta \vec{E} - \frac{1}{c^2} \frac{\partial^2}{\partial t^2} (n^2 \vec{E}) = \frac{4\pi}{c^2} \frac{\partial^2}{\partial t^2} \vec{P}^{\text{NL}}. \quad (1)$$

\vec{E} denotes the total electric field; n is the index of

refraction. The nonlinear polarization \bar{P}^{NL} in Eq. (1) accounts for the interaction of the light field with the material excitation. We make the usual assumptions that the total light field consists of several plane waves with different frequencies and time-dependent amplitudes. The investigated stimulated light scattering occurs very near the forward direction. Stimulated backward scattering is negligible on account of the short duration of the pulses considered here ($\sim 10^{-12}$ sec). For a propagation of the light fields in the x direction we write

$$E(x, t) = \frac{1}{2} \{ E_L \exp[i(k_L x - \omega_L t)] + E_S \exp[i(k_S x - \omega_S t)] \} + \text{c.c.} \quad (2)$$

The subscripts L and S refer to the incident laser field and the generated Stokes field, respectively. Higher-order Stokes and anti-Stokes components are omitted in Eq. (2); this assumption is correct since we restrict the present discussion to a small Stokes conversion of a few percent.

The interaction between the electromagnetic field and the vibrating molecules is described by the nonlinear polarization P^{NL} , which is proportional to the polarizability tensor $\partial\alpha/\partial q$ and the vibrational coordinate q . Extending earlier results^{10,11} to the case of several molecular species j of number density N_j (e.g., isotope components), we introduce the expectation value $\langle q_j \rangle$ of the displacement operator q_j of the individual components and find for the nonlinear polarization P^{NL}

$$P^{\text{NL}} = \frac{\partial\alpha}{\partial q} E \sum_j N_j \langle q_j \rangle. \quad (3)$$

The Raman polarizability $\partial\alpha/\partial q$ is taken to be isotropic, i.e., our calculation refers to highly polarized Raman lines. It has been shown in Ref. 10 that the vibrational amplitude $\langle q_j \rangle$ of the molecular species j obeys the material equation

$$\frac{\partial^2}{\partial t^2} \langle q_j \rangle + \frac{1}{\tau} \frac{\partial}{\partial t} \langle q_j \rangle + \omega_j^2 \langle q_j \rangle = \frac{1 - 2\bar{n}}{2m} \frac{\partial\alpha}{\partial q} E^2. \quad (4)$$

ω_j represents the transition frequency of the individual molecular component j . \bar{n} denotes the small occupation probability of the upper vibrational state, $\bar{n} \ll 1$. For simplicity we assume equal values for the dephasing time τ , the reduced molecular mass m , and for the coupling parameter $\partial\alpha/\partial q$ of the various species j . Equation (4) describes the coherent interaction of a molecular vibration with a coherent light field, assuming a two-level system; this is well justified by the anharmonicity of the molecular vibrations. The quantum-mechanical expectation value $\langle q_j \rangle$ representing the vibrational excitation can be visualized in the classical picture as ensemble average of the vibration-

al displacement q_j ; $\langle q_j \rangle$ contains the phase and amplitude of the individual oscillating molecular component. In a manner similar to that used for the light fields, we write for the vibrational excitation

$$\langle q_j \rangle = \frac{1}{2} Q_j \exp[i(k_j x - \omega_j t)] + \text{c.c.} \quad (5)$$

The wave vector k_j describes the collective vibration within the excited volume; k_j represents the phase relation between the molecules at different points x in the sample. Neglecting second-order derivatives, Eqs. (1)–(5) lead to the following set of differential equations for the generation of the Stokes pulse and the vibrational excitation in the transient stimulated Raman process:

$$\left(\frac{\partial}{\partial x} + \frac{1}{v_S} \frac{\partial}{\partial t} \right) E_S = i\kappa_1 E_L \sum_j N_j Q_j^* \exp(-i\Delta\omega_j t), \quad (6)$$

$$\left(\frac{\partial}{\partial t} + \frac{1}{2\tau} \right) Q_j = i\kappa_2 E_L E_S^* \exp(-i\Delta\omega_j t), \quad (7)$$

where we use the abbreviations

$$\kappa_1 = \frac{\pi\omega_S^2}{c^2 k_S} \frac{\partial\alpha}{\partial q}, \quad \kappa_2 = \frac{\partial\alpha}{\partial q} [4m(\omega_L - \omega_S)]^{-1}. \quad (8)$$

$\Delta\omega_j = \omega_L - \omega_S - \omega_j$ denotes the frequency mismatch between the frequency difference $\omega_L - \omega_S$ of the light fields driving the individual vibrational component and the resonance frequency ω_j . Phase matching $k_j = k_L - k_S$ is established for all species in the stimulated excitation process.

In order to show the physical concept we first discuss the limiting case of a very short excitation pulse, where $|\Delta\omega_j t_p| \ll 1$. It is readily seen from Eqs. (6) and (7) that in this case the factors $\exp(-i\Delta\omega_j t)$ are approximately equal to unity and may be neglected. As a result, the coherent amplitudes Q_j build up according to Eqs. (6) and (7) with equal gain, and we obtain $|Q_j| = Q$. In addition, the short excitation pulse prepares the different molecular species with approximately equal initial phases.

When the incident pump pulse has passed the medium the stimulated excitation process rapidly terminates within a time $t \lesssim t_p$ and the molecular components relax freely. Equations (5) and (7) yield the following time dependence:

$$\langle q_j \rangle \propto \exp(-i\omega_j t) \exp(-t/2\tau),$$

i.e., the collectively vibrating components oscillate with their resonance frequencies ω_j and they decay with the dephasing time τ . For vibrational species of constant frequency difference $\Delta\omega$, a beating phenomenon is expected with maxima occurring after time intervals of $2\pi/\Delta\omega$.

We discuss now the excitation process with moderately short pulses, $|\Delta\omega_j t_p| \lesssim 1$. This case cor-

responds to the experimental conditions discussed below. Introducing a phase factor Φ_j for the individual vibrational component, $Q_j \propto \exp i\Phi_j$, we expand Eqs. (6) and (7) to first order in the factors containing the various phases Φ_j and arrive at the following set of equations:

$$\left(\frac{\partial}{\partial x} + \frac{1}{v_s} \frac{\partial}{\partial t}\right) E_s = \kappa_1 N E_L Q, \quad (9)$$

$$\left(\frac{\partial}{\partial t} + \frac{1}{2\tau}\right) Q = \kappa_2 E_L E_s, \quad (10)$$

$$\frac{\partial \Phi_j}{\partial t} + \frac{\kappa_2 E_L E_s}{Q} (\Delta\omega_j t + \Phi_j) = 0, \quad (11)$$

$$Q_j = iQ \exp(i\Phi_j), \quad (12)$$

$$\omega_s \approx \omega_L - \sum_j N_j \frac{\omega_j}{N}. \quad (13)$$

$N = \sum_j N_j$ is the number density of molecules, v_s denotes the group velocity of the Stokes pulse, and E_L , E_s , and Q represent real quantities without loss of generality. Equations (9) and (10) show that phase-dependent terms have canceled in first order. As a result, the individual components are excited with equal absolute value Q of the vibrational amplitude [see Eq. (12)]. Equations (9) and (10) are identical to the case of a single vibrational mode; they can be solved independent of Eqs. (11) and (12); i.e., a Stokes pulse is produced in the same way as in stimulated Raman scattering of a single molecular vibration. Solutions of E_s and Q have been discussed in the literature^{12,13} in terms of Bessel functions of complex argument. The transient stimulated Stokes emission grows as if the small frequency shifts $\Delta\omega_j$ were absent. Knowing E_s and Q the coherent amplitude Q_j of the individual species is evaluated as a function of time with the help of Eqs. (11) and (12). It should be noted that the total number density N enters the stimulated gain factor^{12,16} G in the present calculation: $G = 4\tau\kappa_1\kappa_2 E_L^2 N l$, where l denotes the interaction length [see Eqs. (9) and (10)]. This result differs from the steady-state stimulated Raman process ($t_p \gg \tau$), where the most abundant isotope species $N_{j_{\max}}$ determines the gain factor.

Detailed calculations of the excitation of adjacent vibrational modes via transient stimulated Raman scattering give the following results:

(i) The coherent Stokes emission is centered at the frequency ω_s of optimum gain indicated by Eq. (13). For a symmetric Raman band the Stokes frequency is situated at the center of the band.

(ii) During the stimulated excitation process, the vibrating molecules do not oscillate exactly with their individual resonance frequency. In fact, the situation is similar to the well-known behavior of the harmonic oscillator, which is excited

under off-resonance conditions. Integration of Eq. (11) for the phase factor yields

$$\Phi_j = -\Delta\omega_j t + \psi_j, \quad (14)$$

where

$$\psi_j = \Delta\omega_j \int_{-\infty}^t dt' \exp\left(\frac{t'-t}{2\tau}\right) \frac{Q(t')}{Q(t)}. \quad (15)$$

The molecular species are coherently driven with the frequency difference $\omega_L - \omega_s$ of the total exciting field. The phase factor Φ_j contains the term $-\Delta\omega_j t$, which corrects our ansatz with frequency ω_j [see Eq. (5)]. ψ_j denotes the phase shift between the individual vibration and the driving force; it is only weakly time dependent during the stimulated excitation process. Equations (14) and (15) indicate that the phase factors Φ_j are readily evaluated after the vibrational amplitude Q is determined from Eqs. (9) and (10). It should be noted that $|\psi_j| \ll 2\pi$ is required in order to stay within the range of validity of Eqs. (6)–(15).

The magnitude of ψ_j depends on the ratio t_p/τ , pulse duration to dephasing time. For shorter excitations smaller values of ψ_j are expected. This point is illustrated by the following numerical examples. In the steady-state situation, $t_p/\tau \gg 1$, Eq. (15) yields $\psi_j = 2\Delta\omega_j \tau$. In the transient case we find values of $\psi_j \approx 0.8\Delta\omega_j \tau$, $0.2\Delta\omega_j \tau$, and $0.04\Delta\omega_j \tau$, respectively, for Gaussian pulses of duration $t_p/\tau = 5$, 1, and 0.2.

When the excitation process has terminated, each vibrational component oscillates with its resonance frequency ω_j , and its phase factor Φ_j [see Eq. (14)] reaches a constant value ($t \geq t_p$)

$$\Phi_{j,\infty} = -\Delta\omega_j \frac{\int_{-\infty}^{\infty} dt t E_L E_s \exp(t/2\tau)}{\int_{-\infty}^{\infty} dt E_L E_s \exp(t/2\tau)}. \quad (16)$$

Equation (16) allows us to calculate the well-defined phase relation between the different vibrational components at the beginning of the free relaxation process.

In Fig. 1 the coherent excitation calculated from Eqs. (8)–(15) is presented. Calculations were made for three molecular species of relative abundance 1:0.5:0.5 and the parameter values $\Delta\omega\tau = \frac{1}{2}\pi$, $t_p/\tau = 1$. The parameters chosen are similar to the isotopic line splitting of the tetrahedron vibration of carbon tetrahalides. The vibrational excitation Q_{tot} is represented by the coherent superposition of vibrational states of number density N_j ,

$$Q_{\text{tot}} = \sum_j N_j \langle q_j \rangle / N. \quad (17)$$

$|Q_{\text{tot}}|^2$ is plotted as a function of time in Fig. 1 (solid curve). $t=0$ marks the maximum of the ex-

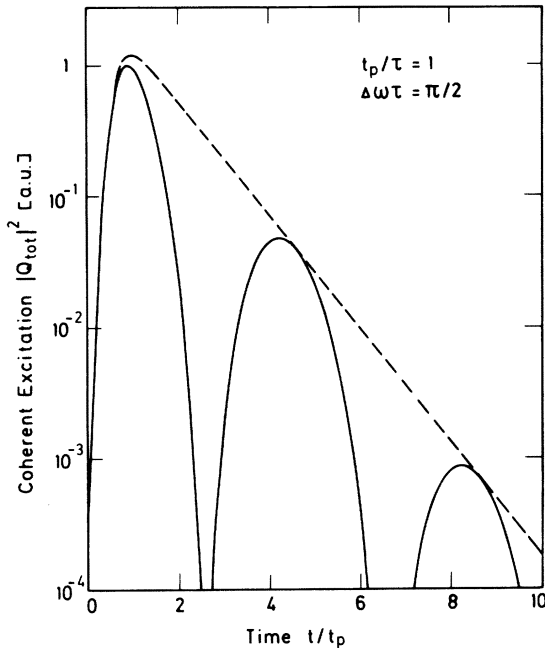


FIG. 1. Calculated coherent vibrational excitation of three molecular species (relative abundance 1:0.5:0.5) as a function of time t/t_p . The solid curve, representing the coherent superposition of vibrational states $|Q_{\text{tot}}|^2 \propto |\sum N_j \langle q_j \rangle|^2$, displays an interesting beating effect; the envelope curve (broken line) indicates the vibrational excitation Q^2 of an individual molecular component. An excitation pulse of Gaussian shape and equal frequency spacing of the vibrational species are assumed.

citation pulse. The vibrational excitation rapidly rises to a delayed maximum at $t/t_p \approx 0.9$. For larger values of t the stimulated process rapidly terminates and the three isotopic components relax freely. It is interesting to see the beating phenomenon which is superimposed on the exponential decay of the vibrational excitation according to the dephasing time (note the broken envelope line). The oscillatory behavior shown in Fig. 1 is a direct consequence of the phase relationship established in the excitation process and the frequency spacing $\Delta\omega$ of the isotopic species. The $|Q_{\text{tot}}|^2$ curve in the figure displays the resulting maxima and minima with beat period of $2\pi/\Delta\omega$.

The following question now arises: How can the beating effect be detected? There are three problems connected with the observation of this phenomenon. First, for line splittings of $\Delta\omega \sim 1 \text{ cm}^{-1}$ the beat periods are of the order of 10^{-11} sec , which is beyond the time resolution of standard photodetectors. Second, vibrational modes, which are Raman but not infrared active, do not radiate, and third, the vibrational excitation decays with the dephasing time τ ; i.e., the phenomenon dis-

appears rapidly within 10^{-11} sec in condensed matter. We shall discuss next coherent Raman scattering of probing light pulses which allows the direct observation of the vibrational beating effect.

III. COHERENT ANTI-STOKES RAMAN PROBE SCATTERING

The coherent interaction of a properly delayed probe pulse with the vibrational excitation is treated in this section. The probe wave is scattered by the coherent material excitations, giving rise to the observed anti-Stokes radiation. The electromagnetic field of the probing process has the form

$$E_{\text{pr}} = \frac{1}{2} \left(E_{L2} \exp[i(k_{L2}x - \omega_{L2}t)] - \sum_j E_{ASj} \exp[i(k_{ASj}x - \omega_{ASj}t)] + \text{c.c.} \right). \quad (18)$$

The subscripts $L2$ and ASj refer to the incident probe pulse and the anti-Stokes scattered light, respectively. Propagation into the x direction is assumed; i.e., we consider scattering in the forward direction. Extension to an off-axis scattering geometry will be discussed below. For every vibrational species j we obtain a corresponding anti-Stokes field. A negative sign of the complex amplitudes E_{ASj} was chosen in order to take into account the proper phase of the anti-Stokes field. The interaction of the probe pulse with the coherent vibrational excitation is calculated with the help of Eqs. (1), (3), (5), and (18). Using similar approximations as for the derivation of Eq. (6) (the Stokes process) we find for the components E_{ASj} of the anti-Stokes scattered field^{4, 10}

$$\left(\frac{\partial}{\partial x} + \frac{1}{v_{AS}} \frac{\partial}{\partial t} \right) E_{ASj} = -ik'_1 N_j E_{L2}(t - t_D) \times Q_j \exp(i\Delta k_j x), \quad (19)$$

where

$$\Delta k_j = k_{L2} + k_L - k_S - k_{ASj}, \quad \omega_{ASj} = \omega_{L2} + \omega_j. \quad (20)$$

t_D denotes the time delay between the maxima of the pumping and the probing pulse. Group velocity dispersion between the anti-Stokes scattered pulse and the Stokes pulse of the excitation process will be neglected, i.e., $v_{AS} \approx v_S$. This approximation is valid for interaction lengths between probing pulse and vibrational excitation of a few centimeters, a condition which is readily fulfilled in our experiments. On the other hand, color dispersion has to be considered in the last factor of Eq. (19). The wave-vector mismatch Δk_j has a different magnitude for the individual components j . This point is important for the subsequent discussion.

Different values of Δk_j are calculated for the vibrational species of frequency ω_j . [See Eq. (20) with $k_{ASj} = \omega_{ASj} n_{AS}/c$.] It should be recalled that the stimulated Stokes process generates identical wave vectors $k_j = k_L - k_S$ of the material excitation. The factor κ'_1 in Eq. (19) combines several material parameters; it is obtained from the corresponding parameter κ_1 in Eq. (8) replacing ω_S and k_S by ω_{AS} and k_{AS} , respectively ($\omega_{ASj} \simeq \omega_{AS}$).

Equation (19) shows that a coherent anti-Stokes field builds up by the interaction of the probe pulse E_{L2} with the coherent vibrational excitation of the sample. This scattering process affects the vibrational excitation. After the excitation, i.e., for probe pulses delayed by $t_D \gtrsim t_p$, we find

$$\left(\frac{\partial}{\partial t} + \frac{1}{2\tau}\right) Q_m = i\kappa'_2 E_{L2}^*(t - t_D) \times \sum_j E_{ASj} \exp\{-i[\Delta k_j x + (\omega_j - \omega_m)t]\}. \quad (21)$$

We derived Eq. (21) in a manner analogous to the derivation of Eq. (7) in Sec. II. Equation (21) indicates that the generation of the anti-Stokes field leads to a loss of the vibrational component Q_m . This result is expected from energy-conservation arguments of the scattering process; the probe and vibrational quanta produce the anti-Stokes radiation [Eq. (20)].

Two points should be noted concerning the coherent probe scattering technique:

(i) We restrict our discussion to probe pulses of small peak intensity. From Eqs. (19) and (21) it can be shown that negligible loss of vibrational excitation is introduced if

$$4\tau\kappa'_1\kappa'_2 N\Delta l |E_{L2}|^2 \ll 1, \quad (22)$$

where Δl denotes the effective interaction length of the probe scattering. This condition is readily fulfilled in experimental investigations using probe pulses of much smaller intensity than the excitation pulse, $|E_{L2}|_{\max}^2 \ll |E_L|_{\max}^2$. Condition (22) ensures that no disturbance of the vibrational excitation results from the use of the probing light pulse.

(ii) It has to be ascertained that additional nonlinear processes do not generate radiation in the frequency range of interest. In particular, the

probe scattering mechanism has to be distinguished from stimulated four-photon parametric interaction of the excitation and probing light pulses.^{14,15} The latter process can produce radiation at the anti-Stokes frequency position of the probe pulse for times when the excitation and probing light pulses overlap, i.e., for small values of t_D . The four-photon parametric process is not connected with the coherent vibrational excitation and has to be avoided. This difficulty can be eliminated by choosing different polarization directions for the exciting and probing pulses.

Experimentally we observe time-integrated scattering signals. We calculate the coherent anti-Stokes probe signal at the end of the sample ($x = l$):

$$S^{\text{coh}}(t_D) = \frac{c n_{AS}}{8\pi} \int_{-\infty}^{\infty} dt \left| \sum_j E_{ASj} \exp[i(k_{ASj}l - \omega_{ASj}t)] \right|^2. \quad (23)$$

Evaluation of the anti-Stokes components E_{ASj} entering Eq. (23) is carried out by the help of Eq. (19). A general analytic solution is not possible, since $Q(x, t)$ and $\Phi_j(x, t)$ have to be found from numerical calculations. For several special cases, however, approximate expressions can be derived which reveal the relevant properties of the coherent probe signal $S^{\text{coh}}(t_D)$.

The integration of Eq. (19) is facilitated using the properties of stimulated Raman scattering. We know that the coherent vibrational amplitude Q grows approximately exponentially with distance:

$$Q^2 \propto \exp(x/\Delta l). \quad (24)$$

Δl denotes the effective excitation length and is readily estimated for a Raman generator setup. For this experimental situation a large amplification of $\sim \exp 25$ is required to build up the intense stimulated Stokes radiation from quantum noise in a sample of length l ; the excitation length $\Delta l \simeq \frac{1}{25}l$ denotes the interval at the end of the interaction path where the maximum excitation occurs.

Of special interest for relaxation studies is the time region $t_D \gtrsim t_p$, where the excitation process has terminated and where we have constant phases $\Phi_{j,\infty}$. From Eqs. (12), (16), (19), (23), and (24) we find for the coherent probe scattering signal

$$S^{\text{coh}}(t_D) \simeq \frac{c n_{AS}}{2\pi} \kappa_1'^2 \Delta l^2 \int_{-\infty}^{\infty} dt \left| E_{L2}(t - t_D) Q(l, t) \sum_j N_j [1 + (2\Delta k_j \Delta l)^2]^{-1/2} \exp[i(\Delta\omega_j t + \delta_j)] \right|^2, \quad (25)$$

where

$$\delta_j = -\arctan(2\Delta k_j \Delta l) + \Phi_{j,\infty} \quad (26)$$

denotes a phase factor of E_{ASj} . Equation (25) in-

dicates that the probe scattering signal increases quadratically with interaction length Δl , field amplitude E_{L2} of the probing pulse, and coherent vibrational amplitude Q . In addition, the

probe signal S^{coh} is seen to depend strongly on the phase-matching situation via the terms $\Delta k_j \Delta l$. According to Eq. (20), the k -vector mismatch of two neighboring vibrational components (frequency spacing $\Delta\omega$) differs by $\Delta\omega n_{\text{AS}}/c$. As a result the product $(\Delta k_j \Delta l)^2$ may vary strongly for different vibrational species. This fact enables us to obtain different physical information by coherent probe scattering. We will discuss two limiting cases.

a. Superposition of vibrational components. Selecting a short effective interaction length Δl , the k -matching situation can be made very similar for the different vibrational components,

$$|\Delta k_j - \Delta k_{j+1}| \Delta l \ll 1. \quad (27)$$

This condition corresponds to the relation $\Delta\omega \Delta l n_{\text{AS}}/c \ll 1$ for the collinear k -vector geometry. All vibrational species j contribute according to their individual number density N_j if Eq. (27) is valid. We observe directly the superposition of the vibrational species each oscillating with resonance frequency ω_j . Equation (25) now yields for the probe signal

$$S^{\text{coh}}(t_D) = \text{const} \times [1 + (2\Delta k \Delta l)^2]^{-1} \times \int_{-\infty}^{\infty} dt \left| E_{L2}(t - t_D) Q \sum_j N_j \exp(i\Delta\omega_j t + i\delta_j) \right|^2. \quad (28)$$

The sum on the right-hand side of Eq. (28) contains oscillating terms $\propto \cos\Delta\omega t_D$. It is important to note that for the phase-matching condition discussed here the probe signal S^{coh} displays a beating phenomenon originating from the coherent superposition of the excited vibrational components. Since $Q^2 \propto \exp(-t/\tau)$ in Eq. (28), the scattering signal decays with the time constant τ . The magnitude of $S^{\text{coh}}(t_D)$ depends upon the phase mismatch. For $\Delta k \Delta l \lesssim 0.5$ with $\Delta k_j \approx \Delta k$ effective probe scattering will occur.

b. Selection of one vibrational state. Under proper experimental conditions, k -vector matching is achieved for only one vibrational component m , $\Delta k_m \approx 0$, while $\Delta k_j \neq 0$ for $j \neq m$. Now, with the help of a sufficiently large interaction length Δl , we can find a selective phase-matching situation where

$$\Delta k_m \Delta l \ll 1 \text{ and } \Delta k_j \Delta l \gg 1 \text{ (} j \neq m \text{)}. \quad (29)$$

The resulting probe scattering signal is found from Eq. (25), for $t_D \geq t_p$,

$$S^{\text{coh}}(t_D) = \frac{c n_{\text{AS}}}{2\pi} (\kappa'_1 \Delta l N_m)^2 \int_{-\infty}^{\infty} dt |E_{L2} Q|^2 \propto \exp(-t_D/\tau). \quad (30)$$

It is interesting to see from Eq. (30) that contribu-

tions of the vibrational species $j \neq m$ disappeared because of the phase-matching condition. The scattering signal results from a single vibrational component ($j = m$) which is isolated with the help of the highly selective \vec{k} geometry.

The signal decays with the relaxation time τ of the coherent vibrational excitation. It is important to note that selective phase matching allows the measurement of the homogeneous line broadening $1/\tau$ within complicated vibrational distributions.

Typical numerical results for the coherent probe scattering signal $S^{\text{coh}}(t_D)$ are shown in Fig. 2. The physical situation assumed was discussed in context with Fig. 1. Knowing Q_j from numerical solutions of the stimulated excitation process [see Eqs. (12), (14), and (15)], we computed the coherent scattering $S^{\text{coh}}(t_D)$ with the help of Eqs. (19) and (23). The broken line represents the scattering signal for selective phase matching [Eq. (29)] corresponding to an isolated component of the isotopic mixture. The decaying part of the signal curve

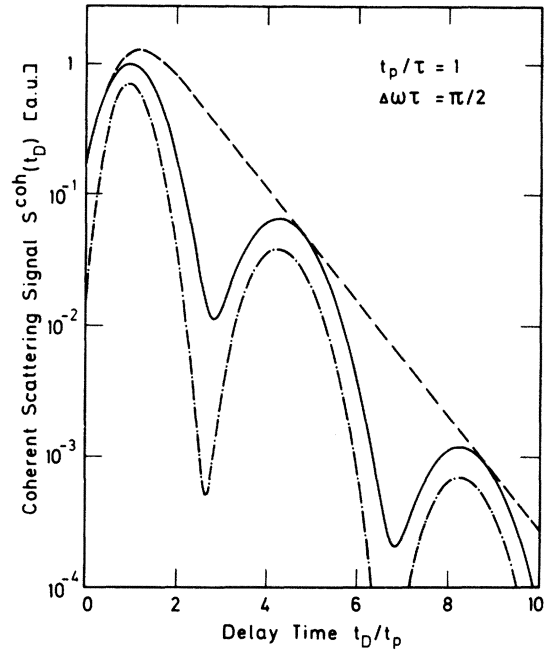


FIG. 2. Calculated probe scattering signal S^{coh} of the vibrational excitation of Fig. 1 as a function of delay time t_D/t_p . The broken curve indicates the scattering signal of an isolated molecular component under selective k -matching conditions. Solid and dash-dotted curves represent the beating effect due to the coherent superposition of the vibrational species calculated for non-selective phase matching. Curves are calculated for probe pulses of Gaussian shape and of duration t_p (solid and broken curves) and $\frac{1}{2}t_p$ (dash-dotted curve).

provides directly the dephasing time τ of the molecular vibration. Probe scattering with nonselective \vec{k} matching is shown by the solid curve in Fig. 2. It is interesting to see the minima and maxima of $S^{\text{coh}}(t_D)$ which reflect the beating phenomenon of the coherent vibrational excitation; the beats occur with time intervals of $2\pi/\Delta\omega$. Comparison of the vibrational excitation (Fig. 1) and the probe scattering (Fig. 2) shows less-pronounced minima of $S^{\text{coh}}(t_D)$. This result is explained by the finite duration t_p of the probe pulse in the probing process. To illustrate this point the scattered signal is calculated for two durations of the probe pulse, t_p and $\frac{1}{2}t_p$ (t_p is the pulse duration of the pumping pulse). Stronger oscillations of the signal curve result from shorter probe pulses.

IV. WAVE-VECTOR GEOMETRIES

It is apparent from the previous sections that the phase-matching situation between the probe pulse and the \vec{k} 's of the material excitation are of major importance for the generated scattered signal. We now discuss in more detail the angular dependence of the generated coherent anti-Stokes signal. It will be shown that the proper choice of phase matching and observation geometry allows the selective observation of one molecular component. With this technique the dephasing time of one isotope species was studied while the neighboring four-isotope components did not contribute to the measured scattered signal.

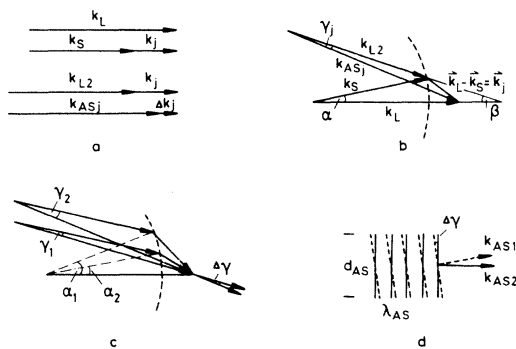


FIG. 3. Wave-vector geometries of the excitation and probing processes (schematic). (a) Collinear geometry; (b) noncollinear \vec{k} matching with probe angle β between excitation (k_L) and interrogating pulse (k_{L2}), and for Stokes emission angle α ; (c) noncollinear \vec{k} matching for two vibrational species; the anti-Stokes emission occurs under different angles γ_1 and γ_2 with respect to the incident probe beam; (d) wave fronts of the interfering anti-Stokes beams.

In Fig. 3(a) the collinear \vec{k} geometry is depicted. Parallel laser and Stokes waves produce the wave vector $\vec{k}_j = \vec{k}_L - \vec{k}_S$ of the material excitation which also points in the forward direction. The probe pulse with parallel wave vector \vec{k}_{L2} coherently interacts with the vibrational excitation generating scattered light in the forward direction with wave vector \vec{k}_{AS} . This geometry is convenient for theoretical descriptions of the probing process; its experimental verification, on the other hand, turns out to be difficult. The wave-vector mismatch Δk_j [compare Eqs. (20), (27), and (29)] can be varied for a given sample by changing the wavelengths of the excitation and probing pulses.

Phase matching can be achieved for the noncollinear wave-vector geometry in Fig. 3(b). It is known that in the stimulated Raman process Stokes light is generated within a cone of small angles α with respect to the forward direction.¹⁶ One roughly estimates that Stokes gain occurs for $\alpha < d/2l$, where d denotes the beam diameter of the laser pulse. Corresponding to the cone of wave vectors $\vec{k}_s(\alpha)$ the vibrational excitation of component j displays a distribution of wave vectors $\vec{k}_j(\alpha) = \vec{k}_L - \vec{k}_s(\alpha)$ of different directions. Note that the magnitude of $|\vec{k}_j(\alpha)|$ depends on the off-axis angle α , while the values of $|\vec{k}_L|$ and $|\vec{k}_s(\alpha)|$ are independent of α and are determined by their frequencies and indices of refraction, $k_{L,S} = \omega_{L,S} n_{L,S}/c$. The interaction of the incident probe pulse (\vec{k}_{L2}) with this cone of material wave vectors $\vec{k}_j(\alpha)$ depends on the resulting mismatch $\Delta k_j(\alpha)$. The angle between the exciting and interrogating beam is denoted by β in Fig. 3(b). For a proper choice of probe angle β , perfect matching $\Delta k_j(\alpha_{j,\text{opt}}) \approx 0$ can be achieved for part of the \vec{k} distribution. These wave vectors $k_j(\alpha \approx \alpha_{j,\text{opt}})$ contribute dominantly to the probe scattering. The highly collimated anti-Stokes emission occurs under angle γ_j with respect to the probe pulse [see Fig. 3(b)]. Experimentally the angles α , β , and γ_j amount to a few degrees. Equations (19), (23), (28), and (30) derived for the probe signal $S^{\text{coh}}(t_D)$ are approximately valid for these small angles.

As an example we consider now the phase matching geometry for two different vibrational species labeled 1 and 2. Figure 3(c) shows schematically that the probe pulse (\vec{k}_{L2}) has to interact with \vec{k} 's of different directions of the two vibrational excitations in order to make $\Delta k_j \approx 0$. As a result, the anti-Stokes wave vectors \vec{k}_{AS1} and \vec{k}_{AS2} of the two vibrational components have slightly different angles γ_1 and γ_2 , respectively. The anti-Stokes scattering signal contains different information as a function of emission angle γ with respect to the incident probe pulse. Using highly collimated beams of the excitation and probing pulses, and

selecting the angle of acceptance with the help of an aperture, the angular dispersion of the probe scattering can be used to isolate a single vibrational component.

For a sufficiently large angle of acceptance the light beams scattered from different vibrational species are simultaneously detected. Beating of the vibrational states corresponds to the interference of the anti-Stokes field components. Figure 3(d) illustrates the situation for two vibrational species. It is readily seen that the resulting scattering signal depends on the beam diameter d_{AS} and the angle $\Delta\gamma = \gamma_1 - \gamma_2$ between the anti-Stokes components. For a beam diameter

$$d_{AS} < \lambda_{AS} / \Delta\gamma, \quad (31)$$

phase differences of the interfering beams at different points of the instantaneous wave fronts in Fig. 3(d) are of minor importance, i.e., a beating phenomenon [Eq. (28)] can be observed. Using green probe light ($\lambda \approx 0.5 \mu\text{m}$) and $\Delta\gamma = 10^{-3}$ we estimate $d_{AS} < 500 \mu\text{m}$. Experimentally we are able to work with beam diameters as small as $30 \mu\text{m}$.

Figures 4(a) and (b) illustrate the phase matching of the probe scattering process. Pump and probe beams of equal frequency $\nu_L = \nu_{2L} = 18910 \text{ cm}^{-1}$ and the physical situation of the symmetric tetrahedron vibration of SnBr_4 at 30°C are considered. The two isotopes ^{79}Br and ^{81}Br produce five lines around 221 cm^{-1} in the vibrational spectrum of this substance (see below). Figure 4(a) refers to parallel pump and probe beams $\beta = 0$. The wave-vector mismatch $\Delta k_j = |\vec{k}_{L2} + \vec{k}_L - \vec{k}_S| - k_{ASj}$, calculated from refractive index data,¹⁷ is plotted in Fig. 4 as a function of the Stokes emission angle α for the five-isotope components j

$= 1-5$. It is readily seen that the Δk_j curves display minima in forward direction $\alpha = 0$ and rise significantly with increasing Stokes angle. Four species display perfect phase matching $\Delta k = 0$, at Stokes emission angles of $\alpha_{\text{opt}} \approx 1.8, 7.3, 10.0,$ and 12.6 mrad , respectively. It is interesting to note that color dispersion incidently leads for the component $j = 4$ to almost perfect phase matching, $\Delta k_4 \approx 0.3 \text{ cm}^{-1}$, in the forward direction, while substantial mismatch, $\Delta k_3 \approx -7.8 \text{ cm}^{-1}$, is found at $\alpha = 0$ for the most abundant isotope component, $j = 3$. This fact can be used for a collinear geometry where the Stokes divergence is made very small (e.g., $\delta\alpha \lesssim 3 \text{ mrad}$) in order to create a highly selective phase-matching situation. Off-axis phase matching for the components $j \neq 4$, on the other hand, does not contribute to the probe scattering, since the required off-axis wave vectors ($\alpha > \delta\alpha$) are not generated in the stimulated excitation process for the small Stokes divergence assumed.

Figure 4(b) shows the phase-matching situation for an angle $\beta = 2.6^\circ$ between pump and probe beam. The wave-vector mismatch Δk_j of the five SnBr_4 species is plotted versus Stokes emission angle α . It is readily seen that the Δk_j curves rise rapidly as a function of Stokes divergence. Phase matching $\Delta k_j = 0$ occurs at different values of Stokes angle α for the individual molecular species j . For example, values of $\alpha = 2.8, 1.9,$ and 1.0 mrad are found, respectively, for $j = 1, 2,$ and 3 in Fig. 4(b). The anti-Stokes probe emission of the individual components occurs in slightly different directions, $\gamma_j = 2.1, 1.3,$ and 0.5 mrad for $j = 1, 2,$ and 3 , respectively. These numbers indicate that coherent superposition for the vibrational components of SnBr_4 may be experimentally observed for the discussed off-axis \vec{k} geometry.

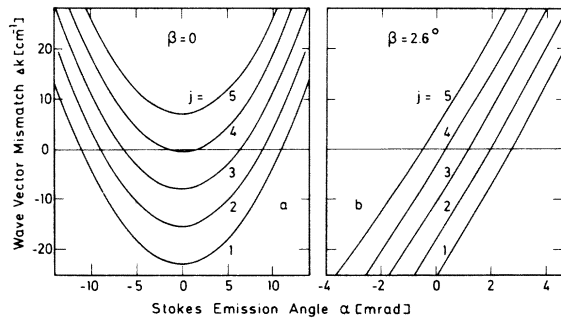


FIG. 4. Wave-vector mismatch Δk of the material excitation and the probing process vs Stokes emission angle α . The tetrahedron modes of the five isotope species of SnBr_4 around 221 cm^{-1} with pump and probe pulses of frequency 18910 cm^{-1} are considered. (a) Parallel excitation and probing beams, $\beta = 0$; (b) probe angle $\beta = 2.6^\circ$; note the different abscissa scales.

V. EXPERIMENTAL

Our experimental systems for coherent probe scattering with off-axis and collinear wave-vector geometry are depicted schematically in Figs. 5(a) and 5(b). For the generation of the ultrashort light pulses we use a mode-locked Nd:glass laser system emitting at 9455 cm^{-1} ($\lambda = 1.06 \mu\text{m}$).¹⁸ In order to obtain reliable experimental data, it is important to work with well-defined single picosecond pulses of known pulse duration, pulse shape, peak intensity, and frequency width.¹⁹ The entire mode-locked pulse train cannot be applied in our investigations, since the pulse parameters vary from the beginning to the end of the pulse train.²⁰⁻²² Pulses at an early position of the train are known to display optimum properties.²² In our

experimental setup a single pulse of transform-limited frequency width is cut from the leading part of the pulse train with the help of an electro-optic switch. The selected pulse subsequently passes an optical amplifier with a gain of approximately 100. A KDP crystal converts the pulse frequency to its second harmonic. The important parameters of the excitation and probe pulse are as follows: frequency $\bar{\nu}_L = 18910 \text{ cm}^{-1}$, frequency width $\delta\bar{\nu}_L \approx 5 \text{ cm}^{-1}$, pulse duration $t_p = 3\text{--}4 \text{ psec}$, and approximately Gaussian shape. TEM₀₀-mode emission of the laser system is achieved by a small diaphragm in the oscillator cavity. Satellite pulses on a picosecond time scale are avoided by a contacted dye-cell configuration.²³ The pulse energy of $\sim 1 \text{ mJ}$ and the quality of the mode locking are monitored with a fast photodiode and a traveling-wave oscilloscope with a time resolution of $\sim 0.5 \text{ nsec}$. Pulses which show evidence of satellites are rejected. It should be noted that the reliability and reproducibility of our picosecond pulses have been tested in numerous investigations.²⁴ An experimental time resolution of better than 0.5 psec has been achieved with these ultrashort pulses.²⁵

Figure 5(a) shows the experimental setup with noncollinear wave-vector geometry. The powerful green-light pulse is directed into a cell with the liquid sample. The peak intensity of the pulse is adjusted by a lens of long focal length ($\sim 30 \text{ cm}$) and neutral-density filters. Stimulated Raman scattering is effectively generated in a cell of typically 2 cm . The stimulated Stokes pulse is detected with a fast photodiode, oscilloscope, and suitable filters. The energy conversion efficiency of laser to Stokes emission is kept at a few percent in order to stay within the validity of our calculations. Two beam splitters provide two pulses of small intensity, approximately 10^{-2} of the exciting pulse. One pulse with variable time delay t_D serves as an interrogating pulse. It interacts with the instantaneous coherent vibrational excitation in the sample. Coherent anti-Stokes Raman scattering is observed close to the forward direction with the help of a grating spectrometer and photomultiplier. The spectrometer serves as a transmission filter for the anti-Stokes frequency position, with a bandwidth of approximately 20 cm^{-1} . An aperture determines the solid angle of acceptance of the detection system. The second weak light pulse (not seen in Fig. 5) with fixed time delay is used to produce a reference scattering signal improving the accuracy of the measurement. The optical delays were carefully determined taking the group velocities in the optical components into account. The accuracy of the t_D scale is better than 2%. The phase matching of the

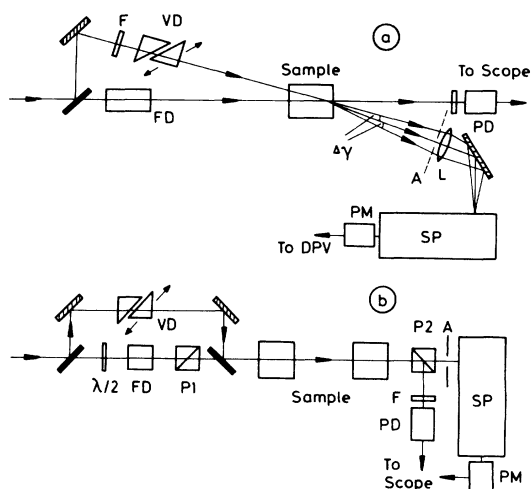


FIG. 5. Experimental systems (schematic) of the coherent probe scattering technique, showing (a) off-axis and (b) collinear wave-vector geometry. A single picosecond pulse enters from the left-hand side. Variable delay VD, fixed delay FD, filter F, $\frac{1}{2}\lambda$ plate, polarizer P, lens L, photodiode PD, spectrometer SP, photomultiplier PM, and digital peak voltmeter DPV are shown. Selective \vec{k} matching may be achieved for the noncollinear geometry (a) with the help of the aperture A and for the collinear geometry and (b) with sufficiently long sample cells.

probe scattering depends considerably on the color dispersion and Raman shift (i.e., vibrational frequency) of the specific sample. The relevant experimental parameters which determine the desired off-axis \vec{k} -matching situation are sample length l , beam diameter d (determining the interaction length Δl and the Stokes divergence $\delta\alpha$), probing angle β , and solid angle of detection $\Delta\Omega$; experimentally we typically have $\delta\alpha \approx 2^\circ$ and $\beta \approx 3^\circ$.

In Fig. 5(b) a different setup used for the collinear wave-vector geometry is depicted schematically. A single picosecond pulse at $\bar{\nu}_L = 18910 \text{ cm}^{-1}$ enters the experimental system from the left-hand side and serves as an excitation pulse. Stimulated Raman scattering is generated in two liquid cells of length $\frac{1}{2}l$ each. The double-cell configuration has the advantage of producing a highly collimated Stokes emission in the forward direction. The amplification process proceeds in two steps. The first cell serves as a Raman generator and produces a (weak) Stokes pulse which acts as a input signal for the amplification in the second cell. Only the Stokes emission of the first cell, which travels within the laser beam, is amplified in the second cell; i.e., the Stokes divergence $\delta\alpha$ is determined by the path length $L+l$ in the generator-amplifier setup. The angle $\delta\alpha$ is estimated to be $\delta\alpha \approx d/2(L+l)$, in

good agreement with experimental findings. For $L=40$ cm, $l=10$ cm, and a beam diameter d of approximately 2 mm a very small Stokes divergence of better than 3 mrad was experimentally observed in SnBr_4 . The Stokes pulse is monitored with a fast photodiode and an oscilloscope. The total conversion efficiency of laser to Stokes light is kept at a value of a few percent.

The probing pulse is generated with the help of a beam splitter; it is properly delayed in a variable-delay system. A second beam splitter allows the probe pulse to travel collinearly with the exciting pulse through the medium. In this way, we work with a probing angle $\beta=0$. The intensity of the probe pulse is less than 1% of the excitation pulse. The interrogating pulse interacts with the coherent vibrational excitation, which is strongest in the second liquid cell. The coherent probe scattering in the forward direction is measured by a grating spectrometer and a photomultiplier. An aperture controls the solid angle of acceptance of the detection system. It should be noted that emission at the anti-Stokes frequency is also produced during the stimulated Raman scattering of the pump pulse.¹⁶ This disturbing background signal is effectively eliminated (factor $>10^5$) with the help of two crossed polarizers $P1$ and $P2$, shown in Fig. 5(b). The exciting and interrogating beams have perpendicular polarization direction. The spectrometer accepts only the scattered anti-Stokes signal produced by the probing pulse. Spontaneous Raman spectra were measured with standard systems consisting of cw-Ar lasers and photon counting techniques.

VI. RESULTS AND DISCUSSION

Our ideas of the superposition of vibrational states and the selection of individual isotope components were tested by experimental investigations of a number of well-known molecules. Liquid tetrahalides were chosen for this paper. The isotope effect of Cl and Br gives rise to vibrational multiplicity of the totally symmetric tetrahedron vibration. Stimulated Raman scattering of these highly polarized vibrational modes is readily achieved on account of the large scattering cross sections. The isotopic line structure of the spontaneous Raman spectrum has been extensively studied for some of these compounds.^{26,27} Figure 6(a) presents an example. The line shape of the tetrahedron A_{1g} vibration of CCl_4 around 459 cm^{-1} is depicted. Distinct line splitting due to the natural abundance of the two chlorine isotopes ^{35}Cl and ^{37}Cl is readily seen. The frequency spacing of the isotopic species is approximately 3 cm^{-1} . The molecular components C^{35}Cl_4 (1), $\text{C}^{37}\text{Cl}^{35}\text{Cl}_3$

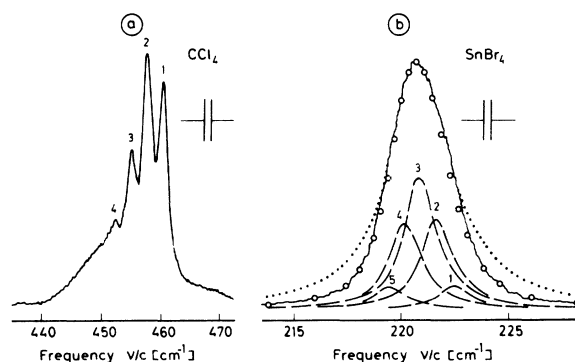


FIG. 6. (a) Spontaneous Raman spectrum of the totally symmetric tetrahedron mode of CCl_4 ; the isotopic line splitting is clearly resolved. (b) The same as in Fig. 6(a), but for SnBr_4 at 305 K (solid curve). The band shape differs notably from a Lorentzian line (dotted curve). The broken curves represent the Raman lines of the individual isotope species and were calculated with the help of our picosecond data. Summation of the five isotope components (open circles) accounts well for the measured spontaneous Raman band (see text).

(2), $\text{C}^{37}\text{Cl}_2^{35}\text{Cl}_2$ (3), and $\text{C}^{37}\text{Cl}_3^{35}\text{Cl}$ (4) have concentration ratios of 0.772:1:0.486:0.105, in agreement with the respective Raman line intensities in Fig. 6(a).²⁶ The fifth component C^{37}Cl_4 is not resolved in the Raman spectrum at room temperature. The significant overlap of lines in Fig. 6(a) should be noted; this overlap does not allow an accurate measurement of the linewidth of a single-isotope component.

Considerably different is the situation for liquid SnBr_4 at 305 K, where the tetrahedron mode around 221 cm^{-1} is shown in Fig. 6(b). A substructure of the Raman band owing to the natural abundance of the ^{79}Br and ^{81}Br isotopes does not show up in the spontaneous Raman spectrum. The smooth line shape in Fig. 6(b) presents no evidence of the presumed isotope distribution, which is masked by the homogeneous broadening of the closely spaced isotope components. The wings of the observed band shape differ noticeably from a Lorentzian line (dotted curve). The broken lines in the figure are calculated curves and will be explained below.

Experimental results of the picosecond probing experiment with off-axis wave-vector geometry [Fig. 5(a)] are discussed first. Figure 7(a) presents data on an isolated component of the tetrahedron vibration of CCl_4 with natural isotope abundance at 295 K. Selective phase matching was experimentally adjusted with the help of a small aperture in the probe scattering beam (~ 2 mrad). Sample length was $l=5$ cm. Wave-vector calculations indicate that the scattered probe emission

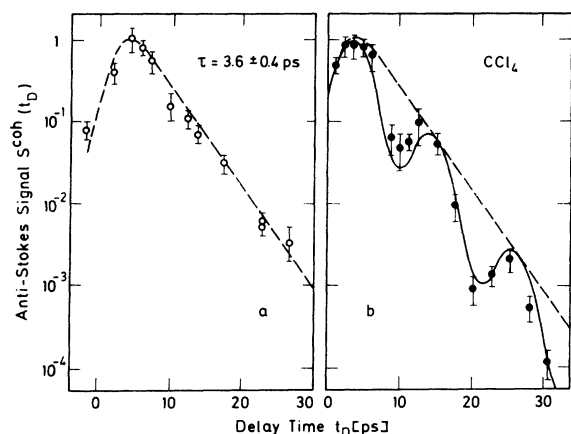


FIG. 7. Coherent probe scattering vs delay time t_D of CCl_4 with natural isotope abundance. (a) Selective \mathbf{k} matching observing a single-isotope component; (b) non-selective \mathbf{k} matching with coherent superposition of vibrational states. The curves are calculated.

of the different isotopic species occurs in different cones of ~ 2 mrad under slightly different angles $\Delta\gamma \approx 6$ mrad. The observed scattered signal is dominantly generated by the most abundant species $\text{C}^{37}\text{Cl}^{35}\text{Cl}_3$, while the aperture effectively blocks scattering from the other isotopic components of the sample. The coherent probe signal S^{coh} is plotted in Fig. 7(a) as a function of delay time t_D between the interrogating and exciting pulse. $t_D = 0$ marks the maximum of the pump pulse. The experimental points represent average values of approximately ten individual measurements and extend over a factor of approximately 500. The vertical bars denote a rms deviation of approximately 20%. The signal points increase to a maximum at $t_D \approx 5$ psec and decay for larger values of t_D . The delay of the maximum is due to the cumulative nature of the excitation process over the duration of the pump pulse. It is interesting to note the exponential decay of the signal curve, which starts shortly after the stimulated scattering has terminated. From the slope of the decaying part of the signal curve the dephasing time τ is directly obtained. A value of $\tau = 3.6 \pm 0.4$ psec is found from the data of Fig. 7(a), which agrees well with our earlier findings on CCl_4 .⁴ The broken line in the figure is a theoretical curve which is calculated for selective phase matching. No fitting parameter enters the calculation once the dephasing time has been directly determined. The good agreement with our experimental points is emphasized.

Of special interest are the data observed when the aperture A in the probe scattering beam is removed [see Fig. 5(a)]. Now the solid angle of ac-

ceptance is considerably larger (~ 10 mrad); probe scattering components in various directions can be readily detected and are expected to be strongly modulated by the beating of the isotope components. Figure 7(b) presents the data. The coherent probe scattering S^{coh} is plotted versus delay time t_D . The decaying part of the signal curve differs drastically from the data of Fig. 7(a). Two minima and additional maxima of the signal curve are clearly indicated by the experimental data of Fig. 7(b), monitoring the relaxation process over four orders of magnitude. The depth of the minima, which are situated approximately a factor of 10 below the envelope curve (broken line), should be noted. Collective beating of the isotope species of CCl_4 is readily seen in Fig. 7(b). The solid curve is calculated from the theory outlined above for a nonselective phase-matching geometry, taking into account the scattering contributions of the four most abundant isotope species of CCl_4 . Since the dephasing time is determined in an independent experiment [see Fig. 7(a)] the only fitting parameter in the calculation is the frequency distance $\Delta\omega$ between neighboring vibrational components, which is determined with considerable accuracy from the data of Fig. 7(b). A value of $\Delta\omega/2\pi c = 2.9 \pm 0.15 \text{ cm}^{-1}$ is found, which favorably compares with the spontaneous Raman data of Fig. 6(a). The good agreement of the theoretical curve (solid line) and the experimental points in Fig. 7(b) should be noted. The broken line is calculated for a single-isotope component and facilitates the comparison of the data with the situation of Fig. 7(a).

We turn now to our investigations of tetrabromides, where the isotopic effect is noticeably smaller on account of the lower vibrational frequencies and the smaller relative mass effect $\Delta m/m$ of the ^{79}Br and ^{81}Br isotopes. Line splitting is not resolved in the spontaneous Raman spectrum [see Fig. 6(b)]. For $\Delta m/m \ll 1$, the frequency spacing is given by^{9,28}

$$\Delta\omega \approx \frac{1}{8} \frac{\Delta m}{m + \Delta m} \omega. \quad (32)$$

For SnBr_4 the frequency interval of the isotope components is estimated to be $\Delta\omega/2\pi c \approx 0.67 \text{ cm}^{-1}$. This value is smaller than the width of the Raman band [Fig. 6(b)] of $\delta\bar{\nu}_{\text{tot}} \approx 3.2 \text{ cm}^{-1}$ by a factor of approximately 5.

Our picosecond probing technique is capable of resolving and studying a single component of the vibrational mode distribution. As an example, Fig. 8(a) presents data on SnBr_4 . The tetrahedron vibration around 221 cm^{-1} was investigated with the collinear wave-vector geometry of Fig. 5(b). Selective phase matching was achieved using an amplification length of $l = 10 \text{ cm}$ for the stimulated

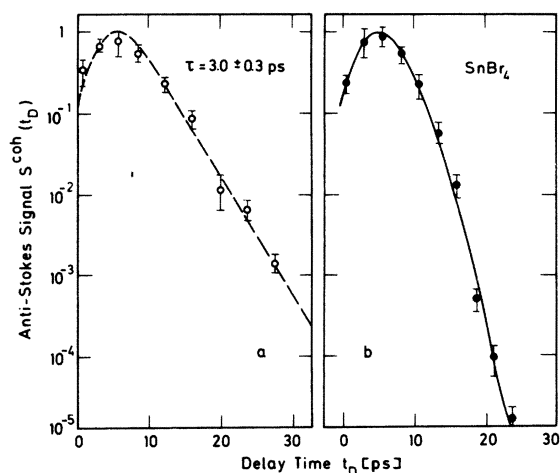


FIG. 8. Same investigations as in Fig. 7, but with SnBr_4 at 305 K. (a) Selective \mathbf{k} matching, observing the homogeneous dephasing time of a single-isotope component. (b) Nonselective \mathbf{k} matching with coherent superposition of vibrational states. Comparison of (a) and (b) directly shows the isotopic substructure of the Raman band, not resolved by spontaneous Raman spectroscopy.

excitation process. The effective interaction length of the probe scattering is estimated to be $\Delta l \approx 0.4$ cm. With the help of Fig. 4(a) the wave-vector mismatch of the component $j = 4$ ($\text{Sn}^{81}\text{Br}_3^{79}\text{Br}$) is found to be $2\Delta k_4 \Delta l \approx 0.24$, i.e., good phase matching is achieved for this vibrational species. For the two neighboring components $j = 3$ and $j = 5$ a value of $2\Delta k \Delta l \approx 6.8$ indicates a significant mismatch of the relevant wave vectors. In fact, a negligible contribution of less than 3% results from these species [see Eq. (25)]. It has been ascertained experimentally that the Stokes divergence of the stimulated excitation process is quite small, $\delta\alpha < 3$ mrad, i.e., off-axis phase matching of the other components ($j \neq 4$) does not contribute in our experiment [see Fig. 4(a)].

The measured probe scattering signal S^{coh} of the isolated isotope species is plotted in Fig. 8(a) versus delay time t_D . The signal rises to a maximum at $t_D \approx 4$ psec and subsequently decreases. It is interesting to see the exponential decay extending over a factor of approximately 500. The dephasing time of the single-isotope component is directly obtained from the slope of the signal curve. A value of $\tau = 3.0 \pm 0.3$ psec is inferred from Fig. 8(a). The broken line has been calculated and favorably accounts for the experimental data. The observed dephasing time corresponds to a homogeneous linewidth of 1.8 cm^{-1} . This value is significantly smaller than the bandwidth of 3.2 cm^{-1} observed in the spontaneous spectrum.

We have studied the same vibrational mode of SnBr_4 with the off-axis geometry of Fig. 5(a) under

nonselective phase-matching conditions. Coherent superposition of the different isotopic components is observed in this case. The picosecond probe data, S^{coh} , are presented in Fig. 8(b). The scattering signal first rises to a maximum level. For longer values of t_D the signal decays rapidly over five orders of magnitude during a time interval of ~ 18 psec. The beat period for SnBr_4 is considerably longer and is estimated to be 50 psec. As a result the signal decays rapidly in Fig. 8(b) but does not reach the first minimum and subsequent maxima of the beating curve. In fact, the beating maximum around $t_D \approx 50$ psec may be expected to be nine orders of magnitude below the peak scattering signal, since the vibrational excitation relaxes quickly with $\tau = 3$ psec [see above and Fig. 8(a)]. Even the large detection range of five orders of magnitude shown in Fig. 8(b) does not allow one to fully observe the beating effect in SnBr_4 . The solid curve in Fig. 8(b) is calculated for the nonselective phase-matching situation using the beat frequency $\Delta\omega$ as a fitting parameter and the measured value of the dephasing time $\tau = 3$ psec which was determined in Fig. 8(a). Good agreement of the theoretical curve with the experimental data (full points) in the figure is obtained for a value of $\Delta\omega/2\pi c = 0.7 \pm 0.15$ cm^{-1} , which favorably compares with theoretical estimates of $\Delta\omega_{\text{th}} \approx 0.67$ cm^{-1} (Eq. 32).

The apparent decay time of the solid curve in Fig. 8(b) of ~ 1.2 psec does not represent a relaxation time of the vibrational system. The observed time dependence results from the destructive interference of the coherently excited vibrational modes. A relaxation time of 1.2 psec would correspond to a spectral linewidth of 4.4 cm^{-1} , which is noticeably larger than the observed spontaneous bandwidth of 3.2 cm^{-1} . The interpretation of our data in terms of the collective beating effect is consistent with time-frequency uncertainty.

The experimental findings of Figs. 8(a) and 8(b) reflect the two limiting cases of selective and of nonselective phase matching. Intermediate situations for the wave-vector geometry were also created experimentally. Correspondingly, the observed curves $S^{\text{coh}}(t_D)$ were situated between the two curves of Fig. 8. These results are well accounted for by theoretical arguments for the coherent probe scattering.

The following points should be noted concerning the data of Fig. 8:

(i) Comparison of the probe-scattering data for different phase-matching conditions (solid and open circles) gives direct experimental evidence of the inhomogeneous substructure of the vibrational system. For a homogeneously broadened line the same time dependence of $S^{\text{coh}}(t_D)$ must occur inde-

pendent of the phase-matching geometry.

(ii) The coherent probe scattering technique allows the direct measurement of the homogeneous linewidth $1/\tau$; this result cannot be obtained from the spontaneous Raman spectrum of SnBr_4 .

(iii) The knowledge of the isotopic line structure is not required to determine the dephasing time τ from the coherent probe scattering data. From the effective interaction length $\Delta l \approx 0.4$ cm, the experimental resolution in k space is estimated to be $\delta k_{\text{instr}} \approx (2\Delta l)^{-1} \approx 1.2$ cm^{-1} , which corresponds to a frequency width of the phase matching of $\delta \bar{\nu}_{\text{instr}} = \delta k_{\text{instr}}/(2\pi n) \approx 0.12$ cm^{-1} for the collinear geometry. These numbers illustrate the high resolution capabilities of the coherent probing technique; $\delta \bar{\nu}_{\text{instr}}$ is smaller than the observed homogeneous linewidth of 1.8 cm^{-1} by a factor of 15 and smaller than the frequency interval $\Delta\omega = 0.7$ cm^{-1} . An individual-isotope component is completely resolved by the large \vec{k} selectivity of the experimental system.

Similar investigations were carried out on SiCl_4 and SnCl_4 . The experimental results are summarized in Table I and compared with the information available from spontaneous Raman spectroscopy. The first two columns list the four liquid tetrahalides and the frequencies of the totally symmetric tetrahedron vibration investigated here. Values of the beat frequency $\Delta\omega$ are indicated in the third column. These numbers were obtained from the beating observed in our coherent probing experiments. The data represent the frequency spacing of the three most abundant isotopic species which dominantly contribute to the observed probe scattering signals. Our experimental data suggest that the values of $\Delta\omega$ are the same for various neighboring isotope components; in fact, detailed models for the isotopic line splitting²⁸ suggest differences for the individual line spacings of only a few percent. Our values of $\Delta\omega$ compare favorably with the spontaneous Raman data of the tetrachlorides (column 4). The considerably higher accuracy should be noted; this makes the picosecond technique particularly well suited for the study of small frequency differences. In SnBr_4 the value

of $\Delta\omega$ cannot be obtained from spontaneous Raman spectroscopy.

The last two columns of Table I present a comparison of our picosecond data on the vibrational dephasing time τ with calculated values from our spontaneous Raman linewidth investigations. For the highly polarized Raman lines investigated, τ is estimated from the linewidth $\delta\bar{\nu}$ (full width at half-maximum in units of cm^{-1}) of the polarized scattering component using the relation^{7,8}

$$\tau = (2\pi c \delta\bar{\nu})^{-1}. \quad (33)$$

Equation (33) is valid for a Lorentzian shape of the spectral line. On account of the overlapping lines, the line shape is not known and only approximate values of $\delta\bar{\nu}$ can be obtained for the individual isotope components [see Fig. 6(a)]. Good agreement is found for the first three compounds in Table I between the estimated data on τ and our coherent probing studies.

For SnBr_4 , on the other hand, the situation is different. The homogeneous linewidth $\delta\bar{\nu}$ cannot be obtained from the spontaneous scattering of this substance. A comparison of our picosecond data in Table I with the spontaneous line shape of SnBr_4 is shown in Fig. 6(b). Knowing the dephasing time τ , the frequency spacing $\Delta\omega$, and the abundance of the SnBr_4 species, the composed spontaneous line shape was evaluated. The exponential decay with $\tau = 3.0$ psec observed in the picosecond investigation corresponds to Lorentzian curves with $\delta\bar{\nu} \approx 1.8$ cm^{-1} [broken lines in Fig. 6(b)]. Natural abundance of the two Br isotopes leads to a relative concentration of the five species $\text{Sn}^{81}\text{Br}_x\text{Br}^{79}\text{Br}_{4-x}$ ($x=0-4$) of 0.173, 0.685, 1.0, 0.653, and 0.160, respectively. Summing up the five isotope lines we obtain the open circles in Fig. 6(b). It is interesting to see that the calculated points account well for the experimental Raman band shape; i.e., our picosecond data are fully consistent with the rather integral information supplied by spontaneous Raman spectroscopy.

Concerning the physics of the dephasing time τ , pure dephasing and energy relaxation have to be considered. It was shown in Ref. 8 that dephasing

TABLE I. Experimental results of four investigated tetrahalides. Center frequency $\bar{\nu}$ of the vibrational system is given, and the measured isotope splitting $\Delta\omega$ and the dephasing time τ are compared with spontaneous Raman data.

	$\bar{\nu}$ (cm^{-1})	$\Delta\omega/2\pi c$ (cm^{-1})		τ (psec)	
		This work	Spontaneous data	This work	From linewidth
CCl_4	459	2.9 ± 0.15	~ 3.0	3.6 ± 0.4	~ 3.8
SiCl_4	425	2.6 ± 0.15	~ 2.5	3.0 ± 0.5	~ 2.8
SnCl_4	368	2.5 ± 0.15	~ 2.9	2.8 ± 0.3	~ 2.5
SnBr_4	221	0.7 ± 0.15	...	3.0 ± 0.3	...

via adiabatic fluctuations of the normal mode frequencies in collisionlike interactions of neighboring molecules plays an important role in the relaxation of molecular vibrations in liquids.

VII. CONCLUSIONS

The experimental data discussed in this paper represent the first observation of the collective beating of molecular vibrations in liquids. The beating phenomenon originates from the coherent superposition of the vibrational amplitudes $\langle q_j \rangle$ of the excited quantum states. $\langle q_j \rangle$ is equal to the expectation value of the displacement operator.¹⁰ There are differences from the quantum beats previously observed in gases²⁹⁻³¹: (i) The different excited states belong to various molecular species; (ii) the vibrational states have no optically allowed transitions, i.e., there is no emission to be observed; (iii) The beat frequency is very high, of the order of 10^{11} sec⁻¹, and the dephasing times are several times 10^{-12} sec. With ultrashort pump

and probe pulses it is possible to study the beating process in the condensed phase.

Observation of the beating effect gives direct experimental evidence for the coherent excitation achieved in the stimulated Raman process; it supports the interpretation of the dephasing time τ in terms of phase relaxation.⁸ The phenomenon is well suited for accurate measurements of small frequency differences. Application of the effect to detailed investigations of isotopic line splitting and of small frequency shifts generated by intermolecular interaction in liquids appears to be a fruitful enterprise.

The collective character of the molecular excitation in the beating effect is emphasized, leading to a high \bar{k} selectivity of the experimental investigations. Our data on SnBr₄ clearly demonstrate the high potential of selective coherent probe scattering. Our new technique allows the investigation of unknown substructures of vibrational lines. New information on vibrational dynamics is provided which is not attainable by other experimental methods.

- ¹A. Laubereau, D. von der Linde, and W. Kaiser, Phys. Rev. Lett. **28**, 1162 (1972).
- ²A. Laubereau, L. Kirschner, and W. Kaiser, Opt. Commun. **9**, 182 (1973).
- ³A. Laubereau, G. Kehl, and W. Kaiser, Opt. Commun. **11**, 74 (1974); A. Laubereau, A. Seilmeier, and W. Kaiser, Chem. Phys. Lett. **36**, 232 (1975).
- ⁴D. von der Linde, A. Laubereau, and W. Kaiser, Phys. Rev. Lett. **26**, 954 (1971).
- ⁵A. Laubereau, Chem. Phys. Lett. **27**, 600 (1974).
- ⁶R. R. Alfano and S. L. Shapiro, Phys. Rev. Lett. **29**, 1655 (1972).
- ⁷A. Laubereau and W. Kaiser (unpublished).
- ⁸S. F. Fischer and A. Laubereau, Chem. Phys. Lett. **35**, 6 (1975).
- ⁹See, for example, G. Herzberg, *Molecular Spectra and Molecular Structure* (Van Nostrand, London, 1968), Vol. 2.
- ¹⁰J. A. Giordmaine and W. Kaiser, Phys. Rev. **144**, 676 (1966).
- ¹¹M. Maier, W. Kaiser, and J. A. Giordmaine, Phys. Rev. **177**, 580 (1969).
- ¹²R. L. Carman, F. Shimizu, C. S. Wang, and N. Bloembergen, Phys. Rev. A **2**, 60 (1970).
- ¹³S. A. Akhmanov, Mater. Res. Bull. **4**, 455 (1969); S. A. Akhmanov, K. N. Drabovich, A. P. Sukhorukov, and A. S. Chirkin, Zh. Eksp. Teor. Fiz. **59**, 485 (1970) [Sov. Phys.-JETP **32**, 266 (1971)].
- ¹⁴N. Bloembergen, in *Nonlinear Optics* (Benjamin, New York, 1965).
- ¹⁵A. Penzkofer, A. Laubereau, and W. Kaiser, Phys. Rev. Lett. **31**, 867 (1973).
- ¹⁶For a review see W. Kaiser and M. Maier, in *Laser Handbook*, edited by F. T. Arecchi and E. O. Schulz-DuBois (North-Holland, Amsterdam, 1972).
- ¹⁷*Gmelins Handbuch der Anorganischen Chemie*, edited by Gmelin Institut (Chemie, Weinheim, 1972), Vol. 46, p. 405.
- ¹⁸For a short survey see A. Laubereau and W. Kaiser, Opto-Electron. **6**, 1 (1974).
- ¹⁹D. von der Linde, O. Bernecker, and W. Kaiser, Opt. Commun. **2**, 149 (1970).
- ²⁰M. A. Duguay, J. W. Hansen, and S. L. Shapiro, IEEE J. Quantum Electron. **QE-6**, 725 (1970).
- ²¹R. C. Eckardt, C. H. Lee, and J. N. Bradford, Appl. Phys. Lett. **19**, 420 (1971).
- ²²D. von der Linde, IEEE J. Quantum Electron. **QE-8**, 328 (1972).
- ²³D. J. Bradley, G. H. C. New, and S. J. Caughey, Phys. Lett. **30A**, 78 (1969).
- ²⁴For a review see A. Laubereau and W. Kaiser, Annu. Rev. Phys. Chem. **26**, 83 (1975); see also Ref. 18.
- ²⁵A. Seilmeier, A. Laubereau, and W. Kaiser, unpublished.
- ²⁶J. Brandmüller, K. Buchardi, H. Hacker, and H. W. Schrötter, Z. Angew. Phys. **22**, 177 (1967); H. H. Eysel and K. Lucas, Z. Naturforsch. A **25**, 316 (1970).
- ²⁷R. J. H. Clark and C. J. Willis, Inorg. Chem. **10**, 1118 (1971).
- ²⁸J. E. Rosenthal, Phys. Rev. **45**, 538 (1934); **46**, 730 (1934).
- ²⁹R. L. Shoemaker and Brewer, Phys. Rev. Lett. **28**, 1430 (1972); W. Gornik, D. Kaiser, W. Lange, J. Luther, and H. H. Schuk, Opt. Commun. **6**, 327 (1972).
- ³⁰S. Haroche, F. A. Paisner, and W. L. Schawlow, Phys. Rev. Lett. **30**, 948 (1973).
- ³¹J. P. Heritage, T. K. Gustafson, and C. H. Lin, Phys. Rev. Lett. **34**, 1299 (1975).